Radically Different Thioredoxin Domain Arrangement of ERp46, an Efficient Disulfide Bond Introducer of the Mammalian PDI Family

Rieko Kojima,[1,7] Masaki Okumura,[1,7,8] Shoji Masui,[1,8] Shingo Kanemura,[2,3] Michio Inoue,[1,8] Masatoshi Saiki,[4] Hiroshi Yamaguchi,[2,3] Takaaki Hikima,[3] Mamoru Suzuki,[5] Shuji Akiyama,[3,6] and Kenji Inaba[1,8,*]

[1]Division of Protein Chemistry, Medical Institute of Bioregulation, Kyushu University, 3-1-1 Maidashi, Higashi-ku, Fukuoka 812-8582, Japan
[2]School of Science and Technology, Kwansei Gakuin University, Gakuen 2-1, Sanda, Hyogo 669-1337, Japan
[3]RIKEN SPring-8 Center, RIKEN Harima Institute, 1-1-1 Kouto, Sayo-cho, Sayo-gun, Hyogo 679-5148, Japan
[4]Faculty of Engineering, Tokyo University of Science, Yamaguchi 756-0884, Japan
[5]Institute for Protein Research, Osaka University, Osaka 565-0871, Japan
[6]Research Center of Integrative Molecular Systems (CIMoS), Institute for Molecular Science, Okazaki 444-8585, Japan
[7]These authors contributed equally to this work
[8]Present address: Institute of Multidisciplinary Research for Advanced Materials, Tohoku University, Katahira 2-1-1, Aoba-ku, Sendai 980-8577, Japan
*Correspondence: kinaba@tagen.tohoku.ac.jp
http://dx.doi.org/10.1016/j.str.2013.12.013

SUMMARY

The mammalian endoplasmic reticulum (ER) contains a diverse oxidative protein folding network in which ERp46, a member of the protein disulfide isomerase (PDI) family, serves as an efficient disulfide bond introducer together with Peroxiredoxin-4 (Prx4). We revealed a radically different molecular architecture of ERp46, in which the N-terminal two thioredoxin (Trx) domains with positively charged patches near their peptide-binding site and the C-terminal Trx are linked by unusually long loops and arranged extendedly, forming an opened V-shape. Whereas PDI catalyzes native disulfide bond formation by the cooperative action of two mutually facing redox-active sites on folding intermediates bound to the central cleft, ERp46 Trx domains are separated, act independently, and engage in rapid but promiscuous disulfide bond formation during early oxidative protein folding. Thus, multiple PDI family members likely contribute to different stages of oxidative folding and work cooperatively to ensure the efficient production of multi-disulfide proteins in the ER.

INTRODUCTION

Oxidative protein folding, coupled with disulfide bond formation, is critical for the proper synthesis of most secretory and cell-surface proteins. While and soon after they are synthesized, such proteins acquire their native structures in the ER, which has multiple pathways for catalyzing formation of disulfide bonds (Bulleid and Ellgaard, 2011; Sato and Inaba, 2012). In the mammalian ER, more than 20 protein disulfide isomerase (PDI) family proteins (Hatahet et al., 2009) and more than five PDI family oxida-

tion enzymes (Araki and Inaba, 2012) constitute a diverse network that greatly promotes oxidative folding of a variety of multi-disulfide proteins, including cell-surface receptors, immunoglobulins, blood coagulation factors, and peptide hormones such as growth factors and insulin.

To fully understand the mechanisms underlying ER quality control, detailed functional characterizations of each oxidative pathway are essential. Recent extensive studies by us and others have clarified that whereas ER oxidoreductin-1α (Ero1α) oxidizes the canonical PDI specifically and efficiently (Inaba et al., 2010; Masui et al., 2011; Wang et al., 2009), Prx4, another ER-resident oxidative enzyme, exhibits significant reactivity toward a broad range of PDI family members (Sato et al., 2013; Tavender et al., 2010). Prx4 has a particular preference for two PDI family members, ERp46 (also known as EndoPDI) and P5, both in vitro and in cultured cells. Importantly, the Prx4-ERp46 and Prx4-P5 oxidative pathways are dedicated to rapid but promiscuous disulfide introduction, suggesting that ERp46 and P5 efficiently catalyze formation of disulfide bonds but lack the ability to introduce native disulfide bonds selectively (Sato et al., 2013). PDI is superior to ERp46 and P5 with respect to selective introduction of native disulfide bonds and can also function as an effective proofreader of non-native disulfide bonds. ERp46/P5 and PDI play distinct roles, acting cooperatively to accelerate proper oxidative protein folding through a process that involves rapid disulfide introduction by ERp46/P5 followed by efficient isomerization of non-native disulfide bonds by PDI (Sato et al., 2013).

Based on the primary sequence of ERp46, this enzyme is predicted to contain three Trx-like domains (Trx1, Trx2, and Trx3), each with a CGHC redox-active site, connected by linker loops of 20 or more amino acid residues (Figure 1A; Figure S1A available online). Although information about the physiological functions of ERp46 is limited, the enzyme has been reported to serve as a stress-survival factor under hypoxia in endothelial cells; furthermore, loss of ERp46 results in reduced secretion of adrenomedullin, endothelin-1, and membrane-bound CD105, suggesting that it is involved in oxidative protein
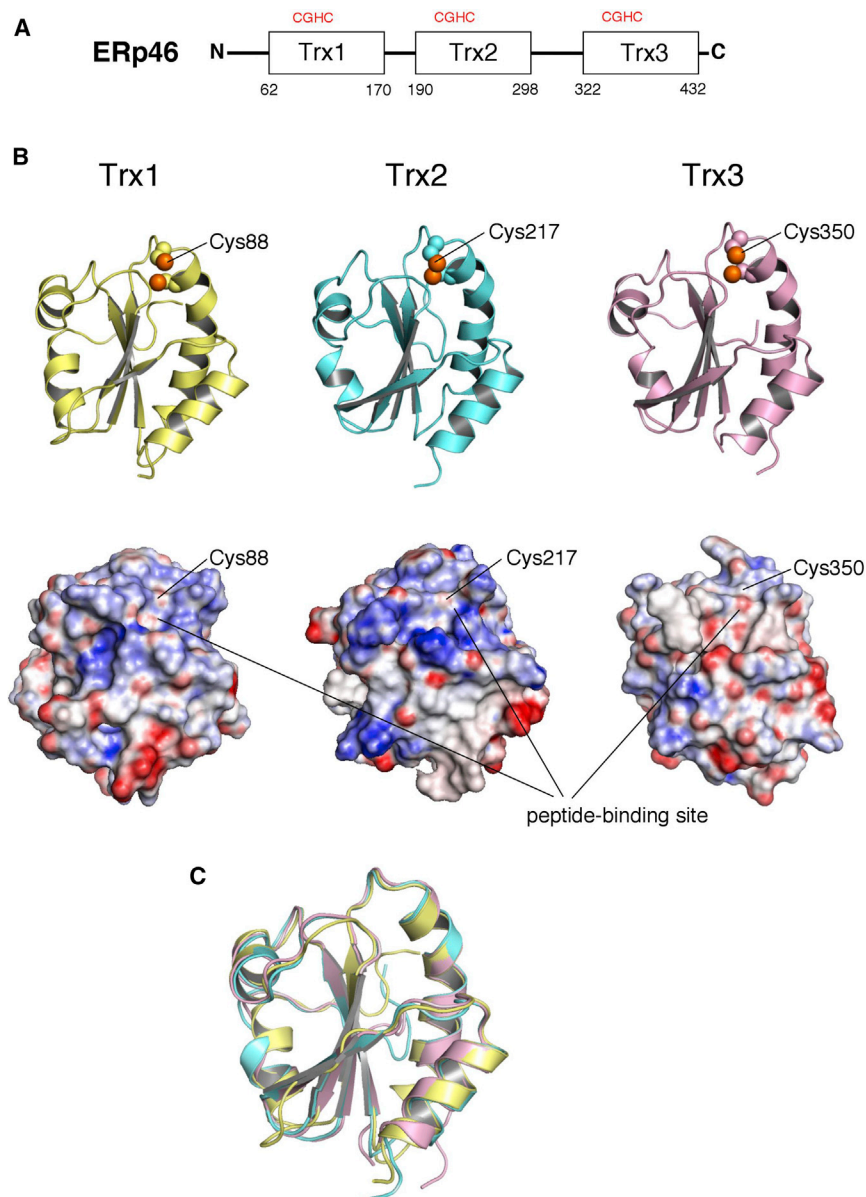
Figure 1. Crystal Structures of ERp46 Trx Domains

(A) Schematic structure of the domain architecture of ERp46. Redox-active Trx domains with a CGHC motif are indicated by Trx1, Trx2, and Trx3, respectively.

(B) Crystal structures of ERp46 Trx domains. Crystal structures of the reduced form of Trx1 (yellow) and oxidized form of Trx2 (blue), both of which were determined in this work, are shown as ribbon diagrams. Crystal structure of Trx3 (PDB ID: 3UVT) is also shown for comparison (light pink). Electrostatic surface of each Trx is displayed below, in which regions of basic potential (>20 k_BT/e) and acidic regions (≤20 k_BT/e) are shown in blue and red, respectively.

(C) Superposition of Trx1 (yellow), Trx2 (blue), and Trx3 (pink) of ERp46. The backbone atoms of these three Trx domains were superimposed such that the RMSD between their Cα atoms was minimized. See also Figure S1.

the overall shape of ERp46 in its reduced and oxidized states in solution. The results demonstrated that the protein exhibits an extended and presumably flexible domain arrangement, irrespective of redox state. These structural features are unique to ERp46, which has a radically different molecular architecture from that of other PDI family members. In agreement with this structural insight, functional analyses demonstrated that each Trx domain acts independently on folding substrates in the Prx4-driven oxidative pathway. The strong preference of Prx4 for ERp46 and the specific oxidation of PDI by Ero1α enabled the efficient recycling of hydrogen peroxide generated by the Ero1α-PDI combination for subsequent re-use in Prx4 catalysis of ERp46 oxidation, which resulted in significant acceleration of proper oxidative protein folding. It is thus conceivable that the mammalian ER has evolved cooperative oxidative pathways involving PDI family members with different structures and different functional roles to ensure the efficient production of large quantities of secretory and cell-surface proteins.

RESULTS

Crystal Structures of the Trx Domains of ERp46

We first sought to crystallize the first and second Trx domains of human ERp46. By molecular replacement using the deposited structure of ERp46 Trx3 (Funkner et al., 2013; Gulerez et al., 2012; Protein Data Bank [PDB] ID: 3UVT) as a search model, we eventually determined their structures at resolutions of 2.5 Å for Trx1 and 0.95 Å for Trx2 (Table 1). The Trx1 crystal belongs to the $P2_1$ space group and contains nine molecules in the asymmetric unit, seven of which are in the oxidized form

folding (Sullivan et al., 2003). Accordingly, ERp46 is preferentially expressed in plasma cells that synthesize and secrete thousands of immunoglobulin M (IgM) pentamers, which contain ∼100 disulfide bonds each, per second (Wrammert et al., 2004). Similarly, ERp46 is involved in insulin production in cultured β cells (Alberti et al., 2009). Proteomic analyses using cysteine-trapping mutants demonstrated that ERp46 forms mixed disulfide complexes with Prx4 and Ero1α, suggesting the occurrence of the Prx4-ERp46 and Ero1α-ERp46 oxidative pathways in human cells (Jessop et al., 2009). Thus, determination of the structure, functions, and mechanisms of operation of ERp46 are of both fundamental and medical importance.

In this study, we investigated the structure and catalytic mechanisms of ERp46. Using crystallographic analyses, we determined the high-resolution structures of Trx1 and Trx2, and in small-angle X-ray scattering (SAXS) analyses, we determined

Table 1. Data Collection and Structure Determination

	ERp46 Trx1 (Mixture of Oxidized and Reduced Form)	ERp46 Trx2 (Oxidized Form)	ERp46 Trx2-Prx4 C-Terminal Peptide Complex
Data Collection			
Beamline	BL44XU at SPring-8	BL44XU at SPring-8	BL44XU at SPring-8
Space group	$P2_1$	$P2_12_12_1$	P1
Cell dimensions (Å)	$a = 50.4$, $b = 94.7$, $c = 142.0$ $\alpha = 90.0°$, $\beta = 90.85°$, $\gamma = 90.0°$	$a = 32.6$, $b = 39.1$, $c = 87.2$ $\alpha = \beta = \gamma = 90.0°$	$a = 35.1$, $b = 36.4$, $c = 40.6$ $\alpha = 81.17°$, $\beta = 87.47°$, $\gamma = 85.40°$
Wavelength (Å)	0.90000	0.70000	0.90000
Resolution range (Å)	35.50–2.50 (2.64–2.50)	12.57–0.95 (1.00–0.95)	26.78–0.92 (0.94–0.92)
No. of total observations	159,099	511,605	364,423
No. of unique reflections	45,514	70,957	126,643
Completeness (%)	98.2 (94.7)	99.9 (100.0)	92.4 (83.0)
$I/\sigma(I)$	7.1 (2.4)	10.9 (3.4)	26.4 (2.0)
Multiplicity	3.5 (3.3)	7.2 (7.1)	2.9 (1.9)
R_{merge}[a]	0.144 (0.549)	0.095 (0.564)	0.053 (0.336)
Refinement			
Resolution range (Å)	34.773–2.500	12.476–0.95	26.785–0.92
No. of reflections	45,487	70,878	126,561
R_{work}[b]	0.1880	0.1222	0.1396
R_{free}[c]	0.2346	0.1348	0.1580
Rmsd			
Bond length (Å)	0.003	0.012	0.013
Bond angle (°)	0.680	1.370	1.500
Ramachandran analysis			
Most favored (%)	98.36	99.3	100.0
Allowed (%)	1.64	0.7	0.0
Disallowed (%)	0.0	0.0	0.0

The number in parentheses represents statistics in the highest-resolution shell.
[a]$R_{merge} = \Sigma\Sigma_j|<I(h)> - I(h)_j| / \Sigma\Sigma_j|<I(h)>|$, where $<I(h)>$ is the mean intensity of symmetry-equivalent reflections.
[b]$R_{work} = \Sigma(||F_p(obs)| - |F_p(calc)||)/\Sigma|F_p(obs)|$.
[c]$R_{free} = R$-factor for a selected subset (5%) of reflections that was not included in prior refinement calculations.

and two are in the reduced form. The Trx2 crystal belongs to the $P2_12_12_1$ space group, and the asymmetric unit contains one molecule with an oxidized active site. Both structures exhibit a prototypical thioredoxin fold composed of a four-stranded β sheet core and four surrounding α helices (Figure 1B, left and middle). As shown in Figure 1C, the backbone atoms of Trx1, Trx2, and Trx3 are almost superimposable on each other, indicating that the main chain structures are extremely similar. However, the electrostatic potential around the peptide binding site differed substantially between the domains: in Trx1 and Trx2, positively charged residues are concentrated near the peptide binding site, whereas in Trx3, the corresponding region is almost neutral (Figure 1B). This finding may account for our recent observation that Trx1 and Trx2 of ERp46 are more efficient substrates for Prx4 than Trx3 (Sato et al., 2013; see also Discussion).

Structural Basis for Recognition of ERp46 Trx Domains by Prx4

We recently reported that the Prx4 C-terminal segment immediately after His244 is responsible for the functional interaction with the N-terminal Trx domain (a^0) of P5 (Sato et al., 2013). In the crystal structure of the P5 a^0-Prx4 C-terminal peptide com-

plex, the Prx4 region Glu246-Gly251 interacts with the peptide-binding site of P5 a^0 via a mixed disulfide bond between a resolving cysteine (Cys248) of Prx4 and an active-site cysteine (Cys57) of P5 a^0 (Figure S2A). To further understand and characterize the mode of interaction between Prx4 and PDI family Trx domains, we carried out a crystal-structure analysis of ERp46 Trx1 and Trx2 in complex with the same Prx4 C-terminal peptide used for the structure of the P5 a^0-Prx4 peptide complex. We succeeded in solving the crystal structure of the ERp46 Trx2-Prx4 peptide complex (Figure 2A). Although the resolution was as high as 0.92 Å, the electron density of the Prx4 peptide was visible only for a limited region between His244 and Ala250, including Cys248, which forms an intermolecular disulfide bond with Cys217 of ERp46 Trx2 (Figure 2B). As in the case of the P5 a^0-Prx4 peptide complex, the Prx4 peptide interacts with a peptide-binding site of ERp46 Trx2 via hydrogen bonding between the guanidinium group of Arg281 (Arg118 in P5 a^0) and the carbonyl group of the main chain of Glu246 (Prx4; Figure 2C). Prx4-catalyzed oxidation of ERp46 Trx2 was greatly slowed down upon the mutation of Arg281Ala (Figure S3), suggesting the important role of this hydrogen bonding in the functional interplay between Prx4 and PDI family members
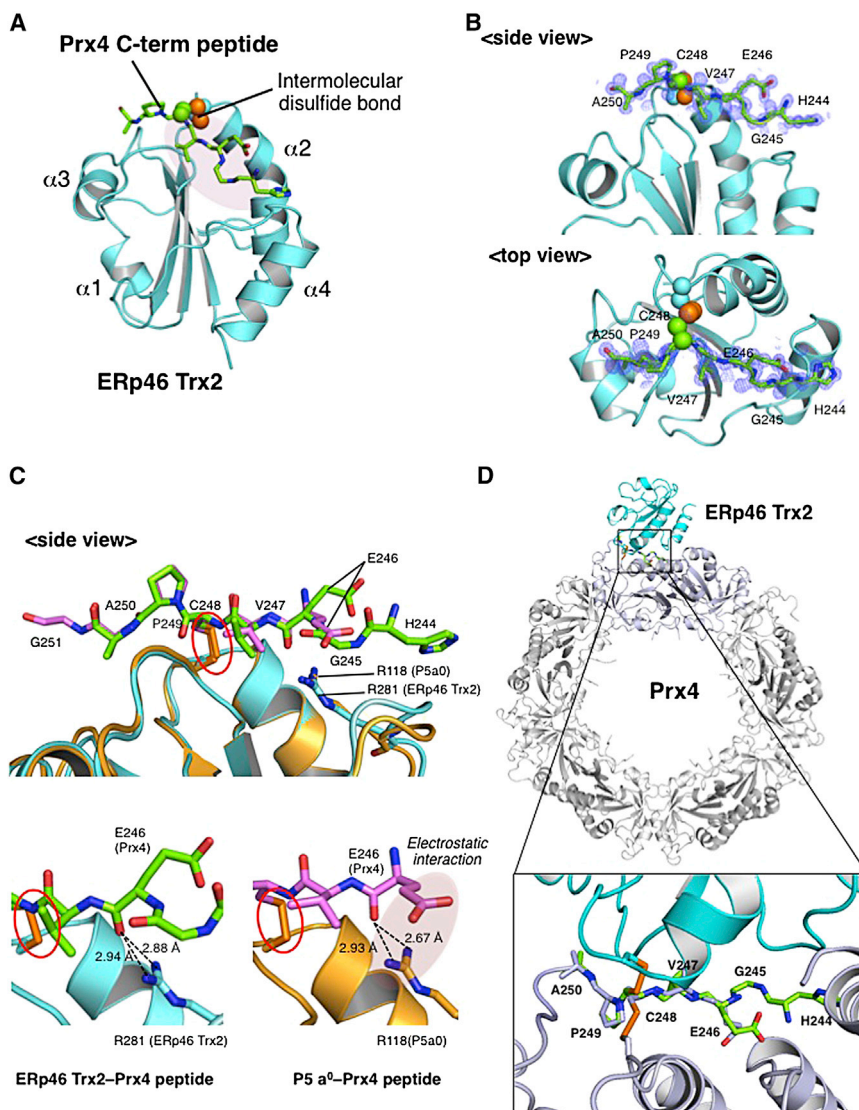
Figure 2. Mode of Interaction between ERp46 Trx and Prx4

(A) Crystal structure of ERp46 Trx2 (cyan; ribbons) in a complex with the Prx4 C-terminal peptide (green; sticks) at 0.92 Å resolution. Cys217 (ERp46) and Cys248 (Prx4 C-terminal peptide), forming the intermolecular disulfide between these two enzymes, are represented by spheres, in which sulfur atoms are colored orange. The peptide-binding site of ERp46 Trx2 is shown as a purple oval.

(B) Close-up views of the interface of the ERp46 Trx2–Prx4 C-terminal peptide complex from two different angles. Electron density map at the 1.0 contour level of the Prx4 C-terminal peptide is indicated with blue mesh.

(C) Comparison of the conformations of the Prx4 peptides bound to ERp46 Trx2 (green) and P5 a^0 (magenta). The intermolecular disulfide formed between the Prx4 peptide and ERp46 Trx2 or P5 a^0 is marked by a red circle. Hydrogen bonds formed between the main chain carbonyl group of Prx4 Glu246 and the guanidinium group of Arg281 in ERp46 Trx2 (lower, left) or Arg118 in P5 a^0 (lower, right) are shown as broken lines in the lower panels. Electrostatic interaction between the side chains of Prx4 Glu246 and P5 Arg118 is displayed as an oval (right, lower panel).

(D) Modeled structure of the ERp46 Trx2–Prx4 decamer complex. The Prx4 C-terminal peptide bound to ERp46 Trx2 is superposed onto the corresponding part of oxidized form of the intact Prx4 decamer (PDB ID: 3VWU) such that the rmsd of their Cα atoms is minimized. The inset shows a close-up view of the interface of the ERp46 Trx2-Prx4 decamer complex, in which the carbon atoms of the Prx4 peptide and intact Prx4 are shown in green and gray, respectively. Note that the bound Prx4 peptide is highly superimposable to the intact Prx4 especially for the segment Glu246-Ala250. For clarity, the view angle is different from that in (C).

See also Figures S2, S3, S6, and S8.

(see also Discussion). However, there are small but significant differences in the interface structures of the P5 a^0-Prx4 peptide and ERp46 Trx2-Prx4 peptide complexes. Whereas in the former the electrostatic interaction occurred between Glu246 (Prx4) and Arg118 (P5 a^0), in the latter, the side chain of Glu246 was oriented in the opposite direction, resulting in the disappearance of the corresponding interaction (Figure 2C). In this connection, the backbone atoms of the N-terminal half of the Prx4 peptide bound to ERp46 Trx2 deviated significantly from those of the peptide bound to P5 a^0 (Figure S2B), and the electron density deriving from His244 and Gly245 completely disappeared in the P5 a^0-Prx4 peptide complex (Figure S2A). Such different structural features of the two complexes may partly explain our recent observation that Prx4 has an ∼5-fold lower affinity for ERp46 than for P5 (Sato et al., 2013).

Using the crystal structures of decameric Prx4 and the ERp46 Trx2-Prx4 peptide complex, we modeled the structure of the Prx4 decamer-ERp46 Trx2 complex in silico (Figure 2D). Notably, the backbone atoms of the Prx4 peptide bound to

ERp46 Trx2 were highly superimposable onto the corresponding atoms in decameric Prx4 (Figure 2D, inset), indicating that no large conformational changes are induced upon formation of a mixed disulfide intermediate complex between ERp46 Trx2 and Prx4. In other words, the C-terminal region of oxidized Prx4 assumes a conformation readily susceptible to nucleophilic attack by Cys217 of ERp46 Trx2. Taken together, the structures of these complexes reveal the common mechanism underlying the recognition of Trx domains of PDI family members by Prx4 and suggest that slight but significant differences in the conformations of the bound Prx4 C-terminal segment may account for differences in the affinities of PDI family members for Prx4.

Small-Angle X-Ray Scattering Analysis of Full-Length ERp46

To determine the domain arrangement and the overall shape of full-length ERp46 in solution, we carried out SAXS analysis. Figure 3A displays the SAXS profiles for the reduced and oxidized forms of ERp46 at infinite dilution (see Figures S4A and S4B
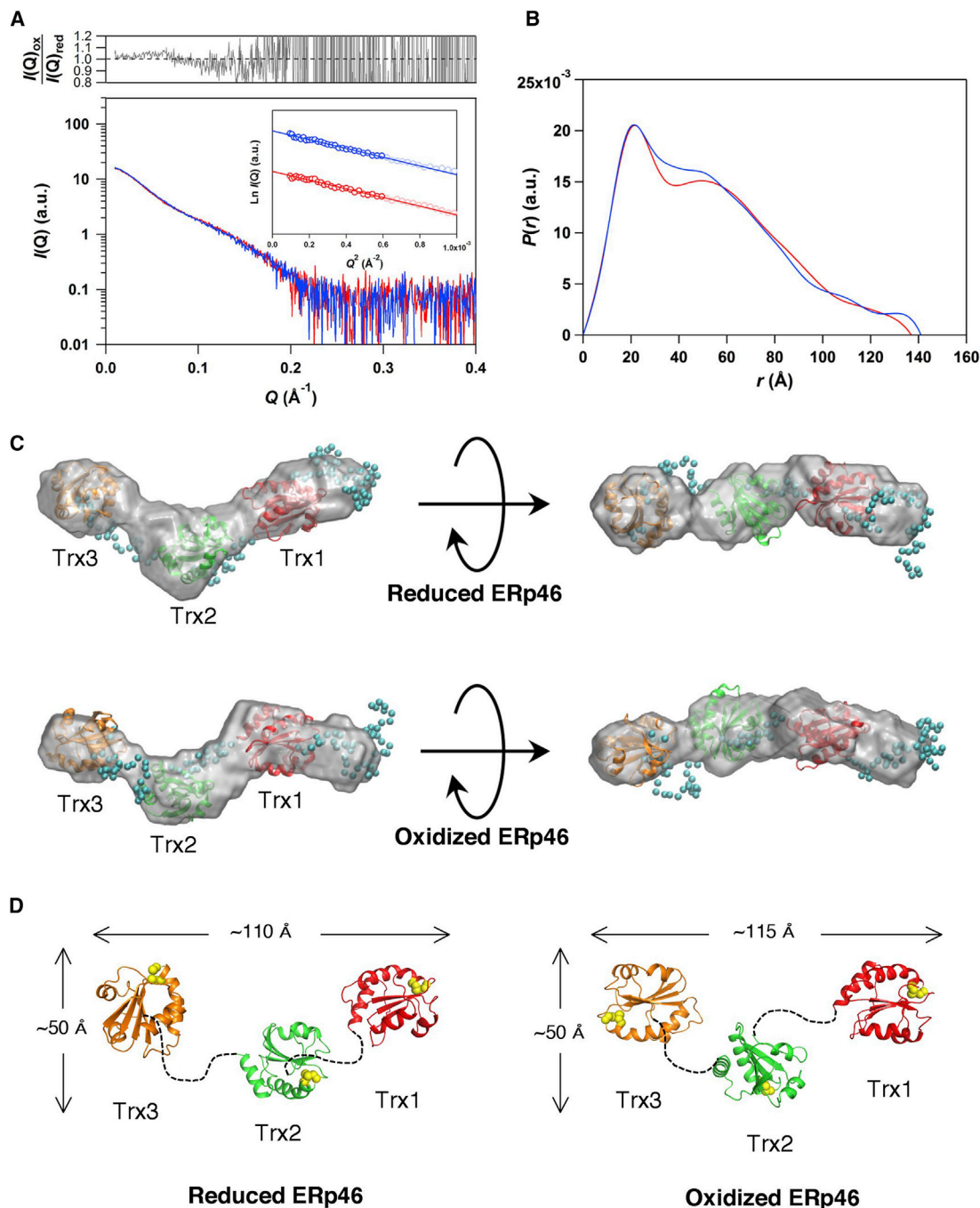
Figure 3. Overall Shapes of Full-Length ERp46 in Reduced and Oxidized States

(A) SAXS curves of reduced (red) and oxidized (blue) forms of ERp46. Natural logarithm of zero-extrapolated scattering intensity, Ln$I(Q)$, is shown as a function of scattering angular momentum, Q. The inset indicates the Guinier plots of reduced (red) and oxidized (blue) forms of ERp46, in which Guinier analyses were conducted using the Q range (highlighted data points in the inset) from 0.00975 Å^{-1} to $Q_{max} < 1.0/R_g$. The upper panel demonstrates an undulated deviation of $I(Q)_{ox}/I(Q)_{red}$ from the unity value.

(B) Pair distribution functions, $P(r)$, of reduced (red) and oxidized (blue) forms of ERp46.

(C) Low-resolution models of the reduced (upper) and oxidized (lower) forms of full-length ERp46 under assumption of quasi-monodispersed distribution (see text). Averaged GASBOR (Svergun et al., 2001) models were depicted as smooth molecular envelopes using the SITUS software package (Wriggers and Chacon, 2001), onto which representative rigid-body refinement models calculated using BUNCH (Petoukhov and Svergun, 2005) were superimposed (see Table 3 for more details).

(D) Representative rigid-body refinement models of reduced (left) and oxidized (right) forms of ERp46 were demonstrated. The CXXC redox active sites in Trx1, Trx2, and Trx3 are shown with yellow spheres.

See also Figures S4–S6.

Table 2. SAXS Structural Parameters

	R_g (Å)[a]	R_g (Å)[b]	$I(0)$ (au)[a]	$I(0)$ (au)[b]	D_{max} (Å)[c]	V_p (Å³)[d]	MM from $I(0)$ (kDa)[e]	MM from V_p (kDa)[f]	MM (kDa)[g]
Reduced ERP46	41.6 ± 0.4	41.8 ± 0.2	16.68 ± 0.07	16.60 ± 0.04	137 ± 5	9.4×10^4	51.0 ± 0.2	57	47
Oxidized ERP46	41.7 ± 0.4	42.0 ± 0.2	17.09 ± 0.06	16.97 ± 0.04	141 ± 6	1.0×10^5	52.2 ± 0.2	61	47
BSA	27.9 ± 0.1	nd	21.70 ± 0.02	nd	nd	nd	nd	nd	66.4

MM, molecular mass; nd, not determined.
[a]Guinier analysis using the Q range from 0.00975 to $Q_{max} < 1.0 / R_g$.
[b]Estimates in real space upon $P(r)$ determination.
[c]Maximum dimension estimated by using GNOM package.
[d]Porod volume.
[e]MM calculated by using the $I(0)$ value for BSA as the standard.
[f]MM calculated according to an empirical relationship (MM = V_P / 1.65; Petoukhvov et al., 2012).
[g]Theoretical MM calculated according to amino acid sequences.

for more details of the concentration dependence). The innermost portion of the Guinier plots (Figure 3A, inset) was linear without any upward curvatures at low Q^2. The radius of gyration R_g and the normalized forward intensity, $I(0)/c$, were determined from the slope and intercept of the linear fits. The R_g values at infinite dilution were estimated to be 41.6 ± 0.4 Å and 41.7 ± 0.4 Å for the reduced and oxidized forms, respectively (Table 2). While the molecular mass of the ERp46 construct used for the SAXS analysis is 47 kDa based on its amino acid sequence (Figure S1B), those estimated from $I(0)$ using BSA as the standard are 51 kDa for reduced form and 52 kDa for oxidized form. The deviations of the estimated molecular mass from the theoretical value (9% to ∼10%) are within the range of the accuracy expected from the interprotein calibration (Akiyama, 2010) and may originate from a slight difference (∼0.01 ml/g) in partial specific volume between ERp46 and BSA. Taken together, both reduced and oxidized forms of ERp46 exist predominantly as a monomer with similar overall structure in solution. This observation is consistent with the recent finding obtained by analytical ultracentrifugation, which revealed that ERp46 exists as a monomer (Funkner et al., 2013).

To gain insights into the molecular shape of full-length ERp46, we calculated a pair distribution function, $P(r)$, using the measured SAXS curves (Figure 3B). The regularization parameter was determined by indirect transform methods using perceptual criteria (Svergun, 1991, 1992). Because $P(r)$ denotes the distributions of linear distances (r) between every pair of atoms in a particle, the most frequent r value and the largest r value (D_{max}) can be determined from the $P(r)$. The D_{max} values of ERp46 were thus estimated to be 137 ± 5 Å for the reduced form and 141 ± 6 Å for the oxidized form (Table 2), suggesting the marginal difference in overall structure upon oxidation of the redox-active sites (Figure 3C).

To draw the overall structure of ERp46 from the SAXS data in an objective manner, we used both the quasi-monodispersed and ensemble-refined models. The representative models built with rigid-body refinement (ribbon models in Figure 3C) and shape reconstructions (smooth envelopes in Figure 3C) demonstrate that the three Trx domains of ERp46 lie in a plane whose dimensions are ∼110 Å × ∼50 Å for the reduced form and ∼115 Å × ∼50 Å for the oxidized form (Figure 3D). Three Trx domains were located apart from each other with very few physical contacts between them, forming an opened V-shape (Figure 3C). Loosely packed domain arrangements implied a flexible

nature of ERp46. Therefore, we next tried to refine ensemble-optimized models (Bernadó et al., 2007) of reduced and oxidized forms of ERp46 using the crystallographic and SAXS data (Figure S5). However, the ensemble models gave rise to only a marginal improvement compared with the fitting using a single rigid-body or shape-reconstruction model (Table 3). Thus, given the flexible nature of ERp46, the degree of conformational freedom is likely limited, and the rigid body and shape reconstruction models can be treated as the representatives of accessible conformational states of ERp46 in solution.

Such separated arrangements of Trx domains are characteristic of ERp46, which has unusually long interdomain linkers and a molecular architecture that is radically different from the known structures of other PDI family members. Notably, the redox-active CXXC motifs of ERp46 Trxs are solvent-exposed and separated from each other (Figure 3D). On the other hand, in PDI and ERp57, the redox-active sites are positioned so that they face each other across the central cleft of the overall "U"-like shape (Dong et al., 2009; Tian et al., 2006; Wang et al., 2012). The different distribution patterns of the redox-active sites in PDI family members lead us to speculate that these proteins may play different functional roles and interact with substrate proteins via different mechanisms (see also the next section).

Using the representative rigid-body model of full-length ERp46 and a model structure of the ERp46 Trx2-Prx4 decamer complex (Figure 2D), we modeled three versions of the ERp46-Prx4 decamer complex, in which Trx1, Trx2, and Trx3 were each placed proximal to the C-terminal region of Prx4 so that they were superposed onto ERp46 Trx2 bound to the Prx4 decamer with the minimal root-mean-square deviation (rmsd; Figure S6). The modeled structures suggested that Trx3 makes slight contact with a part of Prx4 when Trx2 of full-length ERp46 was superimposed to Trx2 bound to Prx4 decamer (Figure S6A). Except for this, there are no gross steric hindrances between Prx4 and ERp46 in any version of the complex. Consistent with this, each Trx domain of ERp46 was oxidized at almost the same rate regardless of whether it was present on an isolated peptide or part of the whole protein (Sato et al., 2013).

Oxidative Folding of BPTI Catalyzed by Prx4 and ERp46 Active-Site Mutants

Our recent functional analyses demonstrated that ERp46 introduces protein disulfide bonds in cooperation with Prx4 more

Table 3. SAXS Shape Reconstruction Statistics for Reduced and Oxidized ERp46 without the N-Terminal Signal Sequence

	Reduced ERp46	Oxidized ERp46
Shape reconstruction	GASBOR2.2i	GASBOR2.2i
Q range ($Å^{-1}$)	0.01002–0.40520	0.01002–0.40520
Real space range (Å)	0–136	0–139
Symmetry	P1	P1
Search space	sphere	sphere
No. of Shannon channels	17.67	17.67
Total number of dummy residues	421	421
SQRT(χ^2) (mean ± SD)	1.244–1.385 (1.294 ± 0.047)	1.151–1.212 (1.182 ± 0.022)
No. of models averaged	10	10
DAMAVER NSD (mean ± SD)	1.207–1.333 (1.271 ± 0.039)	1.197–1.318 (1.236 ± 0.038)
Shape reconstruction	BUNCH08	BUNCH08
Q range ($Å^{-1}$)	0.00975–0.40550	0.00975–0.40550
Real space range (Å)	0–138	0–148
Symmetry	P1	P1
Total number of residues	421	421
Total number of dummy residues[a]	100	100
Dummy residues[a]	1–50, 160–178, 285–311, 418–421	1–50, 160–178, 285–311, 418–421
Total no. of known residues[a]	321	321
Known residues treated as rigid bodies[a]	51–159, 179–284, 312–417	51–159, 179–284, 312–417
SQRT(χ^2) (mean ± SD)	1.181–1.237 (1.216 ± 0.017)	1.168–1.240 (1.190 ± 0.024)
No. of models reconstructed	10	10
DAMAVER NSD (mean ± SD)	1.396–1.678 (1.478 ± 0.090)	1.443–1.729 (1.574 ± 0.089)
Ensemble reconstruction	EOM2.0	EOM2.0
Q range ($Å^{-1}$)	0.00975–0.40550	0.00975–0.40550
Real space range (Å)	0–224	0–242
Symmetry	P1	P1
No. of theoretical curves (pool structures)	10,000	10,000
SQRT(χ^2) (mean ± SD)	1.157–1.159 (1.158 ± 0.001)	1.107–1.110 (1.109 ± 0.001)
Number of ensembles reconstructed	5	5

[a]The residues are numbered based on the amino acid sequence of recombinant ERp46 used for the SAXS measurement (Figure S1B).

rapidly and promiscuously than PDI (Sato et al., 2013). Because the mutation of either one of the CXXC motifs to SXXS compromised even more than 2-fold the activity of PDI to catalyze native disulfide bond formation in buffer containing 1 mM GSH and 0.2 mM GSSG (Walker et al., 1996), the cooperative actions of the two redox-active sites are likely to be optimized for maximal PDI activity. To determine whether this is also true for ERp46, we constructed ERp46 mutants in which only one active site was retained and the other two were mutated to AxxA. As a model

substrate, we used bovine pancreas trypsin inhibitor (BPTI), a protein whose folding pathways have been well characterized in vitro (Arolas et al., 2006). BPTI consists of 58 amino acid residues and contains three intramolecular disulfide bonds (Cys5-Cys55, Cys14-Cys38, and Cys30-Cys51) in the native state. Figure 4A presents a brief scheme of the BPTI oxidative folding pathway mediated by GSH/GSSG, as elucidated in previous in-depth studies (Weissman and Kim, 1991, 1993, 1995).

High-performance liquid chromatography (HPLC) analysis showed that in the presence of externally added H_2O_2, the Prx4-ERp46 combination converted the fully reduced form (R) to oxidized forms within 1 min of refolding time (Figure 4B, left, upper). The HPLC profile displayed a large number of small elution peaks near the peak representing the R form during early refolding times, suggesting that various sorts of intermediates including misbridged species were generated in the initial stages of ERp46-mediated BPTI folding. We thus infer that the Prx4-ERp46 combination allows the BPTI oxidative-folding pathways different from those mediated by GSH/GSSG. Nevertheless, most of these species were ultimately converted to the native state (N) after 60 min of refolding time, despite significant accumulation of the des[30-51] and des[5-55] species (Figure 4B, left, upper).

We next monitored the BPTI folding catalyzed by the ERp46 mutants CxxC-AxxA-AxxA (CAA), AxxA-CxxC-AxxA (ACA), and AxxA-AxxA-CxxC (AAC). All these mutants converted the R species to the N species at almost the same rate as the wild-type (Figure 4B). Likewise, the isolated Trx1, Trx2, and Trx3 domains of ERp46 rapidly introduced disulfide bond(s) into BPTI within 1 min, and converted most of the R form to the N form over the course of a 60 min reaction (Figure S7). These results strongly suggested that the Trx domains of ERp46 work independently of each other in Prx4-driven oxidative protein folding, and that their cooperative or synergistic actions are negligible compared to those of PDI. This finding is compatible with our observation that ERp46 predominantly adopts an extended conformation, in which the three Trx domains are widely separated (Figures 3C and 3D).

Oxidative Folding of BPTI Mediated by Parallel Pathways, Ero1α-PDI and Prx4-ERp46

In previous work, we demonstrated that in contrast to Prx4, Ero1α exhibits strong selectivity for PDI (Inaba et al., 2010; Masui et al., 2011). In this study, we observed oxidative folding of BPTI catalyzed by the Ero1α-PDI oxidative pathway in the presence of saturating levels of molecular oxygen. As shown in Figure 5A, the Ero1α-PDI combination converted R to oxidized species and generated N species more slowly than the Prx4-ERp46 combination (Figure 5A, left). The replacement of PDI by ERp46, a less effective substrate of Ero1α, further slowed down the generation of native species, although the rate of disappearance of R species did not significantly change (Figure 5A, right). Larger numbers of minor elution peaks corresponding to various intermediate species were observed during the ERp46-mediated reaction than during the PDI-mediated reaction, further indicating that ERp46 tends to introduce disulfide bonds promiscuously. In line with this, the folding intermediates, especially des [30-51] and des[5-55], were persistent for longer periods of refolding time in the ERp46-mediated pathway (Figure 5A). Thus,
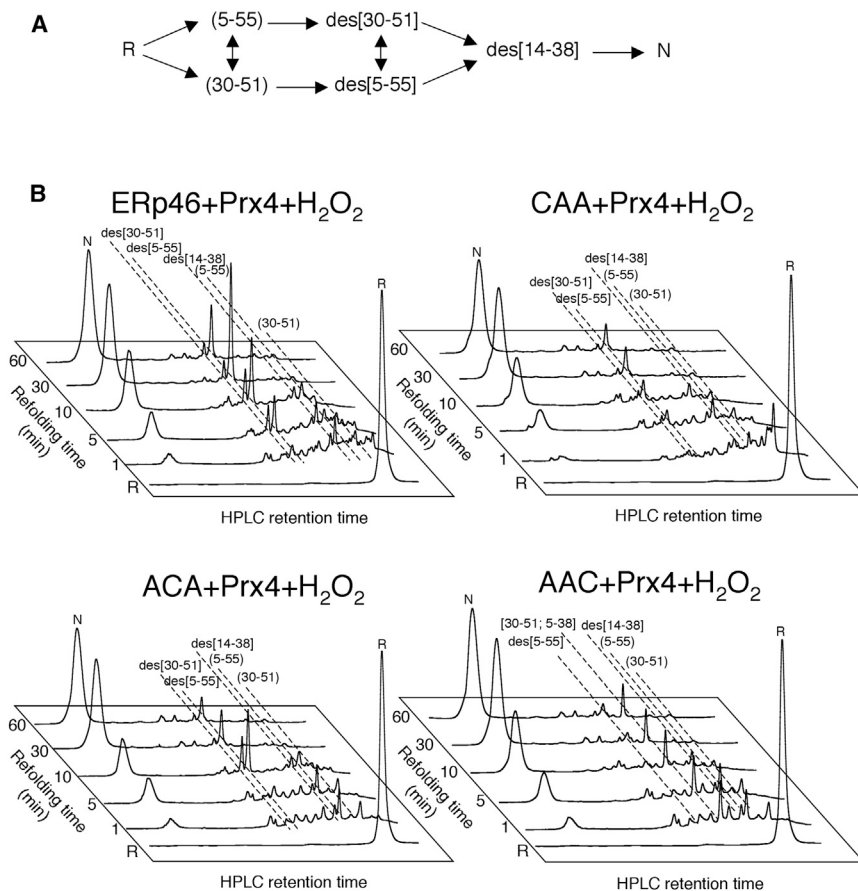
Figure 4. Oxidative Folding of BPTI Catalyzed by Prx4 Combined with ERp46 Mutants

(A) Schematic representation of disulfide-formation pathways for the BPTI folding mediated by GSH/GSSG. R and N indicate the reduced and native BPTI [30-51; 5-55; 14-38], respectively. Initial oxidation of reduced BPTI forms single disulfide intermediates that rearrange (5-55) and (30-51). The disulfide pairings of folding intermediates are shown between parentheses; the missing disulfides between parentheses are indicated with the prefix "des."

(B) HPLC profiles that indicate the time course of oxidative folding of BPTI catalyzed by wild-type ERp46 (left upper), ERp46 mutant CxxC-AxxA-AxxA (CAA; right, upper), AxxA-CxxC-AxxA (ACA; left, lower), or AxxA-AxxA-CxxC (AAC; right, lower). A folding reaction was initiated by the addition of Prx4 (0.1 μM), H_2O_2 (200 μM), and either ERp46 mutants (3 μM) or ERp46 wild-type (1 μM) to reduced BPTI (30 μM). At the selected time points, reaction mixture was quenched with HCl, and analyzed by HPLC. The GSH/GSSG redox reagents were not involved in this reaction assay. Note that the catalysis by the ERp46-Prx4 combination generates various intermediate species with different disulfide bond formation patterns from the ones mediated by GSH/GSSG shown in (A).

See also Figures S7, S9, and S10.

these results clearly indicate that ERp46 is significantly inferior to PDI in recognizing kinetically trapped folding intermediates and converting them to their native states.

Considering that Ero1α catalysis of PDI oxidation yields hydrogen peroxide, we expected that the addition of Prx4 to the Ero1α-PDI oxidative pathway might accelerate oxidative protein folding. However, BPTI folding catalyzed by the Ero1α-PDI combination was not significantly affected by the addition of Prx4 (Figure 5B, left). In contrast, the addition of both ERp46 and Prx4 significantly accelerated the generation of native species (Figure 5B, right). Also, R species decreased sharply between 5 and 10 min during the refolding reaction (Figure 5C). Presumably, the PDI-Ero1α combination yielded hydrogen peroxide during the first 5 min, which was in turn reused by Prx4 to oxidize ERp46 and subsequently convert R to oxidized species. The PDI that remained reduced, or became reduced as a result of BPTI oxidation, likely contributed in the late folding step by recognizing the folding intermediates and efficiently converting them to the native state.

O$_2$ Consumption Mediated by the Ero1α-PDI Oxidative Pathway Is Accelerated by the Presence of the Prx4-ERp46 Pathway

The present observation that the copresence of the Ero1α-PDI and Prx4-ERp46 pathways significantly accelerates oxidative folding of BPTI may suggest that the consumption of molecular

oxygen (O$_2$), an oxidative source for protein disulfide bond formation in this reaction system, is enhanced by the cooperation of Ero1α-PDI with Prx4-ERp46. Indeed, the addition of Prx4 and ERp46 significantly increased the rate of Ero1α-mediated oxygen consumption (Figure 6A). The effect was smaller when ERp46 alone was added, suggesting that the Prx4-ERp46 oxidative pathway facilitates the Ero1α-mediated O$_2$ consumption, presumably through the prompt scavenging of Ero1α-generated H_2O_2 (Figure 6A). A similar observation was made when an ER-resident peroxidase, GPx7 or GPx8, was added to the reaction solution of O$_2$ consumption mediated by Ero1α and PDI (Nguyen et al., 2011; Wang et al., 2013b). The present data suggest that the Ero1α-PDI oxidative pathway can transform the oxidative power of molecular oxygen to native protein disulfide bonds with higher efficiency in cooperation with the Prx4-ERp46 pathway.

DISCUSSION

In this study, we determined the crystal structures of isolated ERp46 Trx1 and Trx2, which revealed that both Trx1 and Trx2, in contrast to Trx3, possess positively charged regions near their peptide-binding sites (Figure 1B). In this regard, it is notable that Prx4 has a negatively charged patch on its surface (Figure S8A). The positively charged patch of ERp46 is predicted to reside near the negatively charged region of Prx4 in the Prx4-ERp46 Trx2 complex (Figure S8B). Thus, the electrostatic interaction seems to play an auxiliary role in the functional interplay between
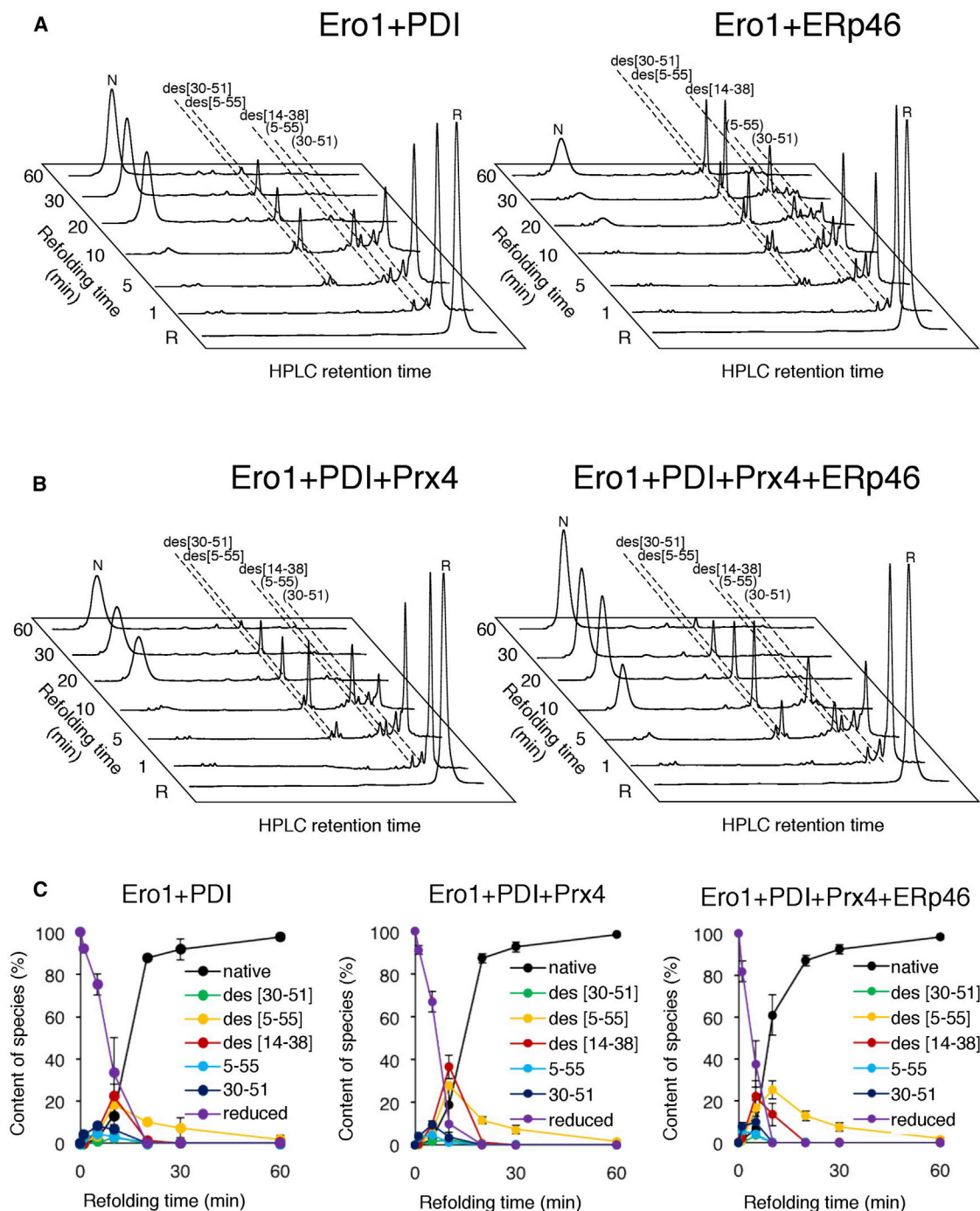
Figure 5. Acceleration of Oxidative Folding of BPTI Mediated by Parallel Pathways, Ero1α-PDI and Prx4-ERp46

(A) Time course of oxidative folding of BPTI catalyzed by combinations of Ero1α with PDI (left) or ERp46 (right). A folding reaction was initiated by the addition of Ero1α (1 μM), and ERp46 or PDI (1 μM) to reduced BPTI (30 μM) in buffer saturated with oxygen (no H_2O_2 added). At the selected time points, reaction mixture was quenched with HCl, and analyzed by HPLC and MALDI-TOF/MS. The GSH/GSSG redox reagents are not involved in this reaction assay.

(B) Time course of oxidative folding of BPTI catalyzed by Ero1α-PDI-Prx4 (left) or Ero1α-PDI-Prx4-ERp46 (right) combinations. Protein concentrations and buffer conditions are as in (A).

(C) Quantitative analyses of the folding intermediates. The occupancy of native, folding intermediates, and reduced species of BPTI were plotted as a function of refolding time. Values are the mean ± SD of three independent experiments.
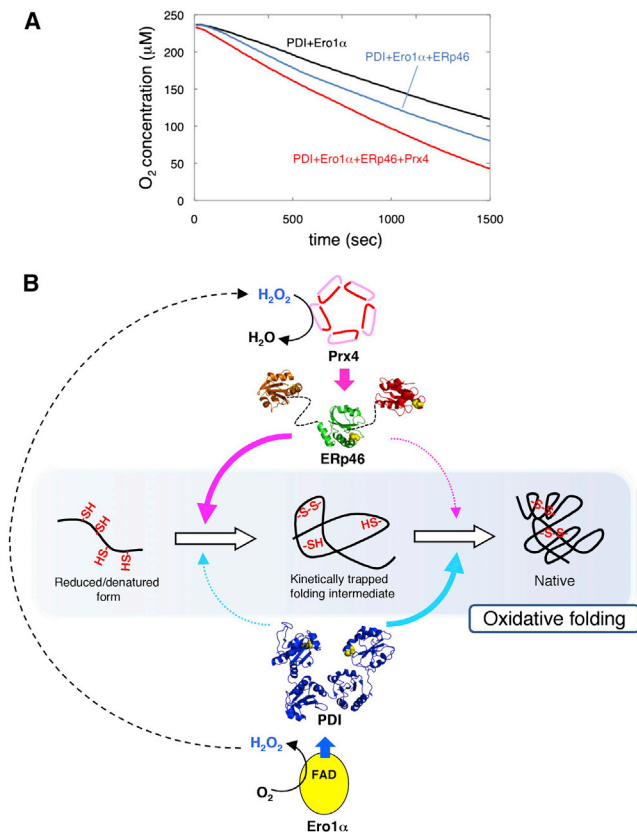
See also Figure S10.

Figure 6. Contributions of the ERp46-Prx4 and Ero1α-PDI Oxidative Pathways in the Different Stages of Oxidative Protein Folding

(A) Oxygen consumption catalyzed by the combinations of Ero1α (1 μM) with 1 μM of PDI (black line), with 1 μM each of PDI and ERp46 (blue line), and with 1 μM each of PDI and ERp46 and 0.1 μM of Prx4 (red line) in the presence of 10 mM reduced glutathione. Note that oxygen consumption is significantly accelerated by the cooperation of Ero1α-PDI and Prx4-ERp46 oxidative pathways.

(B) During the early stages of oxidative protein folding, ERp46 preferentially acts on substrates with unstructured conformations to rapidly introduce disulfide bonds into them. By contrast, PDI tends to recognize kinetically trapped intermediates, eg, "des species," and functions as a terminator of native disulfide bond formation or a proofreader of non-native disulfide bonds to complete the oxidative folding of multi-disulfide proteins.

these two proteins. Meanwhile, the peptide-binding site, which associates with the Prx4 C-terminal peptide, is the region of the primary interaction, in which the guanidinium group of an arginine is hydrogen-bonded to the main chain carbonyl group of Glu246 (Prx4) (Figure 2C). This arginine residue is highly conserved in the Trx domains of PDI family members and a key determinant of the pK_a of the C-terminal cysteine at the active-site CXXC motif (Lappi et al., 2004). The essential role of this arginine in the functional interaction between Prx4 and PDI family members, a finding of this study, suggests that this residue is critically important for efficient disulfide exchange between Prx4 and PDI family members. In support of this, the mutation Arg281Ala in ERp46 Trx2 greatly reduced its reactivity with Prx4 (Figure S3). Presumably, the positively charged side chain of this arginine lowers the pK_a of the C-terminal cysteine at the active site and may promote the nucleophilic attack of

the resultingly deprotonated cysteine on the mixed disulfide between Prx4 and PDI family members.

The representative rigid-body model of ERp46 obtained in our SAXS analysis suggested that the three Trx domains adopt an unusually extended arrangement. By contrast, other PDI family members such as PDI, ERp57, and ERp72 all possess a compact U-shaped structure consisting of four Trx-like domains (**a-b-b′-a′**; Dong et al., 2009; Kozlov et al., 2009; Tian et al., 2006); in this arrangement, the redox-active sites in **a** and **a′** face each other across the substrate-binding hydrophobic cleft constituted by **b** and **b′**. Disruption of either of the redox-active Trx domains (**a** and **a′**) 3- to 4-fold reduces the disulfide isomerase activity of PDI (Walker et al., 1996), suggesting that **a** and **a′** act cooperatively in PDI-mediated oxidative protein folding. Accordingly, the ability of PDI WT to restore the RNase A activity together with Prx4 was much greater than that of the mixture of PDI CxxC-AxxA and PDI AxxA-CxxC (Figure S9B). It is thus conceivable that the cooperative actions of two CxxC active sites contained in a single polypeptide of PDI play an essential role during the Prx4-driven oxidative protein folding. Previous studies reported that rearrangement of Trx domains in PDI is dependent on redox state (Serve et al., 2010; Wang et al., 2013a). Such Trx domain dynamics may help PDI to fulfill its redox and chaperone activities in a manner that is responsive to the redox and folding states of the substrate.

ERp46 has a radically different overall shape than PDI, suggesting that its functions and mechanisms of operation are unique. Indeed, ERp46 hardly showed the cooperative actions of the three CxxC active sites in Prx4-driven oxidative folding of RNase A unlike PDI (Figure S9A). The opened "V"-shape structure, with its marginally hydrophobic surface and widely separated redox-active sites, suggests that ERp46 is deficient in the ability to capture partially structured folding intermediates and rearrange non-native disulfides in such substrates into their native forms with high efficiency. The bacterial homo-dimeric disulfide isomerase DsbC also has V-shaped overall architecture. However, its structural features are rather closer to those of PDI in that the redox-active CXXC motifs face each other across the substrate-binding hydrophobic cleft (McCarthy et al., 2000). The solvent-exposed locations of all of its redox-active CXXC motifs in ERp46 would allow the enzyme to rapidly and promiscuously introduce disulfide bonds into fully or mostly unfolded proteins. The process of nonselective disulfide introduction into unstructured substrates is unlikely to require precise enzyme-substrate recognition, and the diffusive collision of the active-site disulfides of PDI family members with substrate cysteines could be a primary trigger for the introduction of disulfide bonds.

Although PDI is the most effective catalyst for selective oxidation of correct pairs of cysteines, PDI alone would likely not suffice for the efficient production of large quantities of multi-disulfide proteins. High fidelity frequently correlates with low speed; accordingly, PDI-mediated disulfide introduction is precise but time-consuming relative to the ERp46-mediated reaction (Figures 4 and 5). Of note, our recent study demonstrated that cooperation of PDI with ERp46/P5 synergistically accelerates proper oxidative folding of RNase A via rapid but promiscuous disulfide bond introduction by ERp46/P5, followed by immediate proofreading by PDI (Sato et al., 2013). The

addition of GSH did not substantially affect the BPTI folding driven by the Prx4-ERp46 or/and Ero1α-PDI combinations (Figure S10). Thus, it is plausible that the cooperative actions of PDI family members with distinct functional roles could greatly enhance both the rate and fidelity of oxidative protein folding without the assist of GSH, at least in vitro.

In this context, it is notable that Ero1α-generated H_2O_2 could be recycled for use by Prx4 for the catalysis of ERp46 oxidation, leading to the accelerated generation of the native conformer (Figure 5B). Although H_2O_2 is capable of introducing disulfide bonds into PDIs directly (Karala et al., 2009), it has much lower efficiency than the Prx4-catalyzed oxidation of PDIs in the presence of H_2O_2 (Sato et al., 2013). Orchestration of oxygen-consuming and H_2O_2-generating Ero1α with its high specificity for PDI, and H_2O_2-consuming Prx4 with its strong preference for ERp46, is a reasonable strategy for the efficient conversion of the oxidative power of molecular oxygen into native protein disulfide bonds (Figure 6A). ERp46 and PDI contribute to different stages of oxidative protein folding, probably because they have significantly different structural features and hence different functional properties (Figure 6B), as addressed above. Thus, the mammalian ER seems to have evolved a highly organized oxidative network composed of multiple PDI family members with distinct functional roles. The characterization of this network is still incomplete. Future efforts should focus on its complete characterization via global proteomic analysis, which should help shed light on the crosstalk between protein and redox homeostasis in the mammalian ER.

EXPERIMENTAL PROCEDURES

Plasmid Construction, Protein Preparation, and Peptide Synthesis
The procedures of plasmid construction, protein expression and purification, and peptide synthesis are described in the Supplemental Information.

Crystallization of ERp46 Trx1 and Trx2
For crystallization of ERp46 Trx1, protein was concentrated by filtration using Amicon Ultra centrifugal filter units (MWCO, 10,000; Millipore) to approximately 5 mg/ml and dialyzed against 20 mM Tris-HCl (pH 8.1) containing 100 mM NaCl and 1 mM dithiothreitol (DTT). DTT was not removed prior to crystallization. Crystals of ERp46 Trx1 appeared after a few days of vapor diffusion in a sitting drop mode at 20°C in solutions containing 0.1–0.2 M sodium phosphate and 1.2–1.4 M potassium phosphate. For crystallization of ERp46 Trx2, diamide was added to purified Trx2 at a final concentration of 10 mM, and the solution was incubated on ice for 30 min to prepare the fully oxidized form. The sample was loaded onto a Superdex 75 10/300 column in buffer B to remove the diamide. Oxidized Trx2 was then concentrated to approximately 6 mg/ml and dialyzed against MilliQ water (Millipore). Crystals of Trx2 appeared after a week or less of vapor diffusion in a sitting drop mode at 20°C in solutions containing 2.0–2.3 M ammonium sulfate and 100 mM HEPES (pH 7.4–8.0). For cryoprotection, crystals of Trx1 and Trx2 were transferred directly to 20% glycerol premixed in each precipitant solution. Crystals were flash-frozen with cold nitrogen gas from a cryostat (Rigaku).

Preparation and Crystallization of the ERp46 Trx2–Prx4 C-Terminal Peptide Complex
The Trx2 CxxA variant and the Prx4 C-terminal peptide of residues His244-Pro263 were mixed at a 1:4 molar ratio and incubated on ice for 30 min in the presence of 7 mM diamide. The mixed disulfide complex was separated by gel filtration on a Superdex 75 10/300 column pre-equilibrated with 20 mM Tris-HCl (pH 8.1) containing 100 mM NaCl, and concentrated to approximately 6 mg/ml.

The purified complex was vapor-diffused in a sitting drop mode at 20°C under conditions of 18%–22% polyethylene glycol 3350 (PEG3350) and 0.1 M MES-NaOH (pH 6.4–6.6); crystals appeared within a few days. For cryoprotection, crystals were transferred directly to 18% glycerol premixed in precipitant solution and flash-frozen as described above.

Crystallographic Analysis
Diffraction data were collected at the Osaka University beamline BL44XU at SPring-8 equipped with an MX225-HE detector (Rayonix), whose acquisition was financially supported by the Academia Sinica and National Synchrotron Radiation Research Center (Taiwan). For structural determination of ERp46 Trx1 and Trx2, data were integrated with IMOSFLM (Leslie, 2006) and scaled with SCALA from the CCP4 interface (CCP4, 1994). Phase determination was made by molecular replacement using the deposited structure of ERp46 Trx3 (PDB code 3UVT) as a search model with the program Phaser (McCoy et al., 2007). The structures were manually rebuilt with Coot (Emsley and Cowtan, 2004) and refined with Refmac (Murshudov et al., 1997) and phenix.refine. Data collection and refinement statistics are given in Table 1. For structural determination of the ERp46 Trx2-Prx4 C-terminal peptide complex, data were integrated using the HKL2000 software (Otwinowski and Minor, 1997). Phase determination was made by molecular replacement using Phaser, with ERp46 Trx2 (PDB code 3WGE) as a search model. The initial structural models were refined by several cycles of manual rebuilding and refinement with phenix.refine. Figures depicting the structure were prepared with the program PyMOL (Delano Scientific).

Small Angle X-Ray Scattering Experiments
SAXS data were collected at the small-angle X-ray scattering station at the SPring-8 RIKEN beamline (Hyogo, Japan; Fujisawa et al., 2000). The X-ray wavelength was 1.0 Å, and a PILATUS 300K-W system (DECTRIS) was used for detection at a camera distance of about 2,000 mm. The scattering intensity was recorded at 293.2 K as a continuous series of scattering images each taken with exposure time of 10 s for both reduced and oxidized forms of ERp46. Only the images free from radiation damages were averaged to obtain the final data (18 images for either form). During the data collection, the sample was not flowed. The volume of sample measured was 30 μl. A sample solution of reduced form of ERp46 was prepared in 10 mM phosphate buffer (pH 8.0) containing 150 mM NaCl, 5% glycerol, and 1 mM DTT. For preparation of oxidized ERp46, purified ERp46 was incubated in 10 mM phosphate buffer (pH 8.0) containing 150 mM NaCl, 5% glycerol and 5 mM $K_3[Fe(CN)_6]$ on ice for 10 min. After incubation, $K_3[Fe(CN)_6]$ was removed by gel filtration on a Superdex 200 10/300 column. SAXS profiles of ERp46 were collected in the concentration range of 0.6–3.2 mg/ml for reduced form, and of 0.6–3.1 mg/ml for oxidized form. SAXS of bovine serum albumin (molecular weight of 66,400; Sigma-Aldrich) was also collected as a standard for molecular mass determination of ERp46 (Akiyama, 2010). These data treatments resulted in scattering patterns, $I(Q)$, where $Q = 4\pi\sin\theta/\lambda$, 2θ is the scattering angle, and λ is the wavelength of the X-ray. The profiles in the small-angle region were fitted under the Guinier approximation to the equation $I(Q) = I(0)\exp\{-R_g^2Q^2/3\}$, where $I(0)$ is the forward scattering intensity ($Q = 0$) and R_g is the radius of gyration, respectively. The $I(0)$ value is proportional to the averaged molecular mass. Pair-distribution functions, $P(r)$, were calculated by indirect Fourier transformation using GNOM (Svergun, 1991).

Oxidative Folding
BPTI was purchased from Takara Bio. The reduction and denaturation of BPTI were carried out as previously described (Okumura et al., 2011). Fully denatured/reduced BPTI (final concentration, 30 μM) was incubated at 30°C in 50 mM Tris-HCl (pH 7.5) containing 300 mM NaCl in the presence of either 1 μM ERp46, 0.1 μM Prx4, and 200 μM H_2O_2 or 3 μM ERp46 mutant (CAA, ACA, or AAC), 0.1 μM Prx4, and 200 μM H_2O_2. All solutions used in the refolding experiments were flushed with N_2 gas, and the reactions were carried out in sealed vials under an atmosphere of N_2. For aerobic folding of BPTI, the same procedure was used, but the buffer was saturated with oxygen. Reactions were performed at 30°C in 50 mM Tris-HCl (pH 7.5) containing 300 mM NaCl in the presence of 1 μM PDI and 1 μM Ero1α C99A/C104A, a constitutively active mutant of Ero1α; 1 μM ERp46 and 1 μM Ero1α C99A/C104A;

1 μM PDI, 1 μM Ero1α C99A/C104A, and 0.1 μM Prx4; or 1 μM PDI, 1 μM Ero1α C99A/C104A, 1 μM ERp46, and 0.1 μM Prx4.

The reaction mixture was quenched with an equal volume of 1 M HCl. The mixtures were separated on a TSKgel Protein C4-300 (4.6 × 150 mm; TOSOH) at a flow rate of 1.0 ml/min, and monitored at 229 nm. Buffer A is 0.05% trifluoroacetic acid in water, and buffer B is 0.05% trifluoroacetic acid in acetonitrile. In the experiments depicted in Figures 4 and 5, a linear gradient was used: 0 min, 95% buffer A; 15 min, 80% buffer A; and 115 min, 30% buffer A. The occupancy of each folding intermediate at the indicated refolding time was quantified using the software Chrom Merge version 2.2a (GL Sciences).

The molecular mass values of folding intermediates were determined using a DALTONICS autoflex spectrometer (Bruker Japan) in positive-ion mode. Mass spectrometric analyses of proteins were carried out in the linear mode using α-cyano-4-hydroxycinnamic acid (Sigma-Aldrich) as the matrix. Lyophilized sample was dissolved in 0.05% trifluoroacetic acid aq/50% CH₃CN, mixed with a matrix solution (10 mg/ml), and air-dried on the target plate for MALDI-TOF/MS. We calculated the molecular mass values using the Protein-Prospector web server (http://prospector.ucsf.edu/prospector/mshome.htm).

Oxygen Consumption Assay

A Clark-type oxygen electrode (YSI 5331) was used to measure oxygen consumption as previously described (Inaba et al., 2010). All experiments were performed at 30°C in air saturated buffer (approximately 235 μM O₂) in 50 mM Tris-HCl (pH 7.5) containing 300 mM NaCl and 10 mM GSH. Catalytic oxygen consumption was initiated by adding Ero1α C99A/C104A to a final concentration of 1 μM in a reaction mixture containing 1 μM PDI, 1 μM ERp46, and/or 0.1 μM Prx4.

ACCESSION NUMBERS

The PDB accession numbers for ERp46 Trx1, ERp46 Trx2, and the ERp46 Trx1-Prx4 C-terminal peptide complex are 3WGD, 3WGE, and 3WGX, respectively.

SUPPLEMENTAL INFORMATION

Supplemental Information includes Supplemental Experimental Procedures and ten figures and can be found with this article online at http://dx.doi.org/10.1016/j.str.2013.12.013.

REFERENCES

Akiyama, S. (2010). Quality control of protein standards for molecular mass determinations by small-angle X-ray scattering. J. Appl. Cryst. *43*, 237–243.

Alberti, A., Karamessinis, P., Peroulis, M., Kypreou, K., Kavvadas, P., Pagakis, S., Politis, P.K., and Charonis, A. (2009). ERp46 is reduced by high glucose and regulates insulin content in pancreatic beta-cells. Am. J. Physiol. Endocrinol. Metab. *297*, E812–E821.

Araki, K., and Inaba, K. (2012). Structure, mechanism, and evolution of Ero1 family enzymes. Antioxid. Redox Signal. *16*, 790–799.

Arolas, J.L., Aviles, F.X., Chang, J.Y., and Ventura, S. (2006). Folding of small disulfide-rich proteins: clarifying the puzzle. Trends Biochem. Sci. *31*, 292–301.

Bernadó, P., Mylonas, E., Petoukhov, M.V., Blackledge, M., and Svergun, D.I. (2007). Structural characterization of flexible proteins using small-angle X-ray scattering. J. Am. Chem. Soc. *129*, 5656–5664.

Bulleid, N.J., and Ellgaard, L. (2011). Multiple ways to make disulfides. Trends Biochem. Sci. *36*, 485–492.

CCP4 (Collaborative Computational Project, Number 4) (1994). The CCP4 suite: programs for protein crystallography. Acta Crystallogr. D Biol. Crystallogr. *50*, 760–763.

Dong, G., Wearsch, P.A., Peaper, D.R., Cresswell, P., and Reinisch, K.M. (2009). Insights into MHC class I peptide loading from the structure of the tapasin-ERp57 thiol oxidoreductase heterodimer. Immunity *30*, 21–32.

Emsley, P., and Cowtan, K. (2004). Coot: model-building tools for molecular graphics. Acta Crystallogr. D Biol. Crystallogr. *60*, 2126–2132.

Fujisawa, T., Inoue, K., Oka, T., Iwamoto, H., Uruga, T., Kumasaka, T., Inoko, Y., Yagi, N., Yamamoto, M., and Ueki, T. (2000). Small-angle-X-ray scattering station at the SPring-8 RIKEN beamline. J. Appl. Cryst. *33*, 797–800.

Funkner, A., Parthier, C., Schutkowski, M., Zerweck, J., Lilie, H., Gyrych, N., Fischer, G., Stubbs, M.T., and Ferrari, D.M. (2013). Peptide binding by catalytic domains of the protein disulfide isomerase-related protein ERp46. J. Mol. Biol. *425*, 1340–1362.

Gulerez, I.E., Kozlov, G., Rosenauer, A., and Gehring, K. (2012). Structure of the third catalytic domain of the protein disulfide isomerase ERp46. Acta Crystallogr. F. Struct. Biol. & Crystalliz. Comm. *68*, 378–381.

Hatahet, F., Ruddock, L.W., Ahn, K., Benham, A., Craik, D., Ellgaard, L., Ferrari, D., and Ventura, S. (2009). Protein disulfide isomerase: a critical evaluation of its function in disulfide bond formation. Antioxid. Redox Signal. *11*, 2807–2850.

Inaba, K., Masui, S., Iida, H., Vavassori, S., Sitia, R., and Suzuki, M. (2010). Crystal structures of human Ero1α reveal the mechanisms of regulated and targeted oxidation of PDI. EMBO J. *29*, 3330–3343.

Jessop, C.E., Watkins, R.H., Simmons, J.J., Tasab, M., and Bulleid, N.J. (2009). Protein disulphide isomerase family members show distinct substrate specificity: P5 is targeted to BiP client proteins. J. Cell Sci. *122*, 4287–4295.

Karala, A.R., Lappi, A.K., Saaranen, M.J., and Ruddock, L.W. (2009). Efficient peroxide-mediated oxidative refolding of a protein at physiological pH and implications for oxidative folding in the endoplasmic reticulum. Antioxid. Redox Signal. *11*, 963–970.

Kozlov, G., Määttänen, P., Schrag, J.D., Hura, G.L., Gabrielli, L., Cygler, M., Thomas, D.Y., and Gehring, K. (2009). Structure of the noncatalytic domains and global fold of the protein disulfide isomerase ERp72. Structure *17*, 651–659.

Lappi, A.K., Lensink, M.F., Alanen, H.I., Salo, K.E., Lobell, M., Juffer, A.H., and Ruddock, L.W. (2004). A conserved arginine plays a role in the catalytic cycle of the protein disulphide isomerases. J. Mol. Biol. *335*, 283–295.

Leslie, A.G. (2006). The integration of macromolecular diffraction data. Acta crystallographica. Section D. Biol. Crystallogr. *62*, 48–57.

Masui, S., Vavassori, S., Fagioli, C., Sitia, R., and Inaba, K. (2011). Molecular bases of cyclic and specific disulfide interchange between human ERO1alpha protein and protein-disulfide isomerase (PDI). J. Biol. Chem. *286*, 16261–16271.

McCarthy, A.A., Haebel, P.W., Törrönen, A., Rybin, V., Baker, E.N., and Metcalf, P. (2000). Crystal structure of the protein disulfide bond isomerase, DsbC, from Escherichia coli. Nat. Struct. Biol. *7*, 196–199.

McCoy, A.J., Grosse-Kunstleve, R.W., Adams, P.D., Winn, M.D., Storoni, L.C., and Read, R.J. (2007). Phaser crystallographic software. J. Appl. Cryst. *40*, 658–674.

Murshudov, G.N., Vagin, A.A., and Dodson, E.J. (1997). Refinement of macromolecular structures by the maximum-likelihood method. Acta crystallographica. Section D. Biol. Crystallogr. *53*, 240–255.

Nguyen, V.D., Saaranen, M.J., Karala, A.R., Lappi, A.K., Wang, L., Raykhel, I.B., Alanen, H.I., Salo, K.E., Wang, C.C., and Ruddock, L.W. (2011). Two

endoplasmic reticulum PDI peroxidases increase the efficiency of the use of peroxide during disulfide bond formation. J. Mol. Biol. *406*, 503–515.

Okumura, M., Saiki, M., Yamaguchi, H., and Hidaka, Y. (2011). Acceleration of disulfide-coupled protein folding using glutathione derivatives. FEBS J. *278*, 1137–1144.

Otwinowski, Z., and Minor, W. (1997). Processing of X-ray diffraction data collected in oscillation mode. In Methods in Enzymology, C.W. Carter, Jr., ed. (Academic Press), pp. 307–326.

Petoukhov, M.V., and Svergun, D.I. (2005). Global rigid body modeling of macromolecular complexes against small-angle scattering data. Biophys. J. *89*, 1237–1250.

Petoukhov, M.V., Franke, D., Shkmuatov, A.V., Tria, G., Kikhney, A.G., Gajda, M., Gorba, C., Mertens, H.D.T., Konarev, P.V., and Svergun, D.I. (2012). New developments in the ATSAS program package for small-angle scattering data analysis. J. Appl. Cryst. *45*, 342–350.

Sato, Y., and Inaba, K. (2012). Disulfide bond formation network in the three biological kingdoms, bacteria, fungi and mammals. FEBS J. *279*, 2262–2271.

Sato, Y., Kojima, R., Okumura, M., Hagiwara, M., Masui, S., Megawa, K., Saiki, M., Horibe, M., Suzuki, M., and Inaba, K. (2013). Synergistic cooperation of PDI family members in peroxiredoxin 4-driven oxidative protein folding. Sci. Rep. *3*, 2456.

Serve, O., Kamiya, Y., Maeno, A., Nakano, M., Murakami, C., Sasakawa, H., Yamaguchi, Y., Harada, T., Kurimoto, E., Yagi-Utsumi, M., et al. (2010). Redox-dependent domain rearrangement of protein disulfide isomerase coupled with exposure of its substrate-binding hydrophobic surface. J. Mol. Biol. *396*, 361–374.

Sullivan, D.C., Huminiecki, L., Moore, J.W., Boyle, J.J., Poulsom, R., Creamer, D., Barker, J., and Bicknell, R. (2003). EndoPDI, a novel protein-disulfide isomerase-like protein that is preferentially expressed in endothelial cells acts as a stress survival factor. J. Biol. Chem. *278*, 47079–47088.

Svergun, D.I. (1991). Mathematical, ethods in smail-angle scateering data analysis. J. Appl. Cryst. *24*, 485–492.

Svergun, D.I. (1992). Determination of the regularrization parameter in indirect-transform methods using perceptual criteria. J. Appl. Cryst. *25*, 495–503.

Svergun, D.I., Petoukhov, M.V., and Koch, M.H. (2001). Determination of domain structure of proteins from X-ray solution scattering. Biophys. J. *80*, 2946–2953.

Tavender, T.J., Springate, J.J., and Bulleid, N.J. (2010). Recycling of peroxiredoxin IV provides a novel pathway for disulphide formation in the endoplasmic reticulum. EMBO J. *29*, 4185–4197.

Tian, G., Xiang, S., Noiva, R., Lennarz, W.J., and Schindelin, H. (2006). The crystal structure of yeast protein disulfide isomerase suggests cooperativity between its active sites. Cell *124*, 61–73.

Walker, K.W., Lyles, M.M., and Gilbert, H.F. (1996). Catalysis of oxidative protein folding by mutants of protein disulfide isomerase with a single active-site cysteine. Biochemistry *35*, 1972–1980.

Wang, L., Li, S.J., Sidhu, A., Zhu, L., Liang, Y., Freedman, R.B., and Wang, C.C. (2009). Reconstitution of human Ero1-Lalpha/protein-disulfide isomerase oxidative folding pathway in vitro. Position-dependent differences in role between the a and a' domains of protein-disulfide isomerase. J. Biol. Chem. *284*, 199–206.

Wang, C., Yu, J., Huo, L., Wang, L., Feng, W., and Wang, C.C. (2012). Human protein-disulfide isomerase is a redox-regulated chaperone activated by oxidation of domain a'. J. Biol. Chem. *287*, 1139–1149.

Wang, C., Li, W., Ren, J., Fang, J., Ke, H., Gong, W., Feng, W., and Wang, C.C. (2013a). Structural insights into the redox-regulated dynamic conformations of human protein disulfide isomerase. Antioxid. Redox Signal. *19*, 36–45.

Wang, L., Zhang, L., Niu, Y., Sitia, R., and Wang, C.C. (2013b). Glutathione peroxidase 7 utilizes hydrogen peroxide generated by Ero1a to promote oxidative protein folding. Antioxid. Redox Signal. http://dx.doi.org/10.1089/ars.2013.5236.

Weissman, J.S., and Kim, P.S. (1991). Reexamination of the folding of BPTI: predominance of native intermediates. Science *253*, 1386–1393.

Weissman, J.S., and Kim, P.S. (1993). Efficient catalysis of disulfide bond rearrangements by protein disulphide isomerase. Nature *365*, 185–188.

Weissman, J.S., and Kim, P.S. (1995). A kinetic explanation for the rearrangement pathway of BPTI folding. Nat. Struct. Biol. *2*, 1123–1130.

Wrammert, J., Källberg, E., and Leanderson, T. (2004). Identification of a novel thioredoxin-related protein, PC-TRP, which is preferentially expressed in plasma cells. Eur. J. Immunol. *34*, 137–146.

Wriggers, W., and Chacon, P. (2001). Using Situs for the registration of protein structures with low-resolution bead models from X-ray solution scattering. J. Appl. Cryst. *34*, 773–776.